


RESEARCH ARTICLE | AUGUST 14 2023

## Three-dimensional mixed boiling: A strategy for critical heat flux enhancement

Hao Wang (王浩) ; Dongxue Guan (关冬雪); Xianbing Ji (纪献兵)  ; Jinliang Xu (徐进良) 



*Physics of Fluids* 35, 083317 (2023)

<https://doi.org/10.1063/5.0161309>



View  
Online



Export  
Citation

CrossMark



**APL Quantum**  
Bridging fundamental quantum research with technological applications

**Now Open for Submissions**  
No Article Processing Charges (APCs) through 2024

**Submit Today**



# Three-dimensional mixed boiling: A strategy for critical heat flux enhancement

Cite as: Phys. Fluids **35**, 083317 (2023); doi: [10.1063/5.0161309](https://doi.org/10.1063/5.0161309)

Submitted: 9 June 2023 · Accepted: 29 July 2023 ·

Published Online: 14 August 2023



View Online



Export Citation



CrossMark

Hao Wang (王浩),<sup>1</sup>  Dongxue Guan (关冬雪),<sup>1</sup> Xianbing Ji (纪献兵),<sup>1,2,a)</sup>  and Jinliang Xu (徐进良)<sup>1,2</sup> 

## AFFILIATIONS

<sup>1</sup>Beijing Key Laboratory of Multiphase Flow and Heat Transfer for Low Grade Energy Utilization, North China Electric Power University, Beijing 102206, People's Republic of China

<sup>2</sup>Key Laboratory of Power Station Energy Transfer Conversion and System, North China Electric Power University, Ministry of Education, Beijing 102206, People's Republic of China

<sup>a)</sup>Author to whom correspondence should be addressed: [jxb@ncepu.edu.cn](mailto:jxb@ncepu.edu.cn)

## ABSTRACT

To improve the critical heat flux (CHF) in boiling heat transfer, an idea of triggering three-dimensional mixed boiling was proposed, and the corresponding surface with an extended thin film (ETFS) was designed by adding a film structure on the plain surface (PS). With ethanol as working fluid, experiments were conducted to explore mixed boiling heat transfer and CHF enhancement mechanisms on ETFS. The results demonstrate that ETFS induces spatially uneven temperatures on the boiling surface, which triggered mixing boiling in the spatial dimension—the coexistence of nucleate and film boiling—leading to a significant CHF enhancement. Nucleate boiling in the falling liquid along the extended surface is the key to stabilizing the surface temperature during the formation of dry spots on the base surface. Compared with PS and the traditional pin–fin surface, ETFS increased CHF by approximately 110% and 45%, respectively. Analysis indicated that mutual interference between nucleate boiling and film boiling effectively inhibits heat transfer deterioration caused by the deactivation of nucleating points. Through decoupling analysis of the mutual interference process in mixed boiling, it is shown that at heights of 2.0, 4.0, 6.0, and 8.0 mm, the contributions of extended film to total heat transfer are 12%, 64%, 37%, and 24%, respectively, indicating an optimal extended film height of 4.0 mm for maximum boiling heat transfer performance. This novel boiling surface with extended film structure not only improves CHF, but also reduces design costs, offering valuable guidance for radiator design purposes.

Published under an exclusive license by AIP Publishing. <https://doi.org/10.1063/5.0161309>

## I. INTRODUCTION

Pool boiling is a complex phase change heat transfer process occurring in large space. Due to small driving temperature difference and strong heat transfer ability, it has been widely used in the industry, such as cooling of nuclear power reactors,<sup>1</sup> steam generation in thermal power generation,<sup>2</sup> and thermal management of high-power electrical equipment.<sup>3</sup> In 1966, Nukiyama<sup>4</sup> carried out pioneering research on pool boiling. He first discovered the so-called boiling curve and described the boiling process, contributing a lot to the classical theory of pool boiling. In the boiling process, the superheat of the heating surface and the critical heat flux (CHF) are two key parameters to identify the boiling mode. According to surface superheat, steady-state boiling modes are broadly classified into nucleate boiling and film boiling. Nucleate boiling, characterized by high heat flux and low surface superheat, is regarded as the most efficient boiling mode in phase change heat transfer. Conversely, film boiling is accompanied by a low heat transfer coefficient when a steam blanket covers the heating surface, resulting in heat transfer deterioration. The excessive accumulation of

heat during film boiling can result in an uncontrollable and rapid rise in the temperature of the boiling surface.<sup>3</sup> Once surface temperature surpasses the temperature limit of material, it can lead to catastrophic incidents such as component burning accidents.<sup>5</sup> Therefore, it is of great significance to improve CHF and prevent the heating surface from entering the film boiling.

So far, there are many ways to improve CHF. Regarding the boiling surface structure, researchers mostly use mechanical or chemical methods to build different structures on the boiling surface, which can be broadly categorized into microscale structure, nanoscale structure and micro–nano hybrid structure (MNHS). In the microscale range, the pin–fin structure is the most typical, enhancing boiling heat transfer by increasing boiling surface area.<sup>6–8</sup> Compared with the smooth surface, its surface superheat is significantly reduced, benefiting from enhanced intercostal micro-convection and film evaporation. In addition to the pin–fin structure, artificial cavities and sintered structures are also attractive microstructures, capable of enabling effective boiling heat transfer through a combination of steam overflow, liquid

replenishment, and stable nucleation.<sup>9–11</sup> However, such structural surfaces are easily blocked, resulting in increased flow resistance and diminished heat transfer capacity.<sup>12</sup> For the nanoscale boiling surface, nucleation boiling heat transfer is closely related to the surface wettability and pore size.<sup>13</sup> On the one hand, nanostructures can adjust the surface wettability and regulate the liquid supplement during the boiling process.<sup>14,15</sup> On the other hand, it also increases the number of active nucleation sites.<sup>16,17</sup> Although the nanostructure surface has shown significant improvement in heat transfer efficiency, this improvement may not be sustainable due to the final functional degradation caused by the fracture of nanostructures.<sup>18</sup> Moreover, the costly processing requirements pose challenges for industrial applications. Considering the advantages of both microscale and nanoscale structures, the micro–nano hybrid structure (MNHS) has garnered attention in recent years. MNHS exhibits improved liquid rewetting and bubble nucleation, thereby enhancing boiling heat transfer and delaying the onset of the boiling crisis.<sup>19–21</sup> However, it still faces challenges encountered by micrometer and nanoscale structured surfaces discussed above, simultaneously having high preparation costs.

Therefore, some scholars attempt to improve CHF by manipulating bubbles behavior and liquid replenishment. Rahman *et al.*<sup>22</sup> created a double thermal conductivity surface to achieve orderly bubble nucleation by adding low thermal conductivity materials to the liquid–solid interface. They found that when the capillary length of liquid matched the Taylor wavelength, a resonance-like effect occurred, resulting in enhanced heat transfer. Compared with an ordinary surface, CHF can be increased by about 100%. Utaka *et al.*<sup>23</sup> triggered mixed boiling, including nucleate boiling and film boiling on the plain surface (PS) with non-uniform heat conduction. The CHF can be increased by 68%. Building upon these findings, Xie *et al.*<sup>24</sup> and Omisany *et al.*<sup>25</sup> extended this approach to confined pool boiling and flow boiling, and CHF increased by 84% and 43.4%, respectively.

Despite the studies mentioned above successfully demonstrating the mutual interference between nucleate boiling and film boiling in the planar dimension, a challenge arises from the lateral expansion of bubbles across the boundary between low-conductivity and high-conductivity surfaces. This expansion leads to the temporary deactivation of nucleation points and subsequent deterioration of boiling heat transfer.<sup>26</sup> For this reason, an innovative boiling surface with extended film (ETFS) was proposed by adding an extended film structure on the smooth surface. Therefore, the spatially uneven temperature was generated, which can trigger mixed boiling with the coexistence of nucleate boiling and film boiling in the three-dimensional spatial dimension. Due to the mutual interference between nucleate boiling and film boiling, the CHF of whole boiling surface can be enhanced. This study utilizes high-speed visualization and infrared (IR) temperature measurement technology to analyze the contribution of extended surfaces on boiling heat transfer, thereby uncovering the physical mechanism of CHF enhancement. Overall, this study has the potential to introduce a novel and cost-effective surface design for enhancing boiling heat transfer.

## II. TRIGGERING MECHANISM OF THREE-DIMENSIONAL MIXED BOILING

Since the bubble detachment frequency, diameter, and liquid replenishment have an important impact on the boiling heat transfer, better strategies are needed to enhance CHF by controlling the bubble

behavior, surface wettability, and liquid replenishment. Several studies (Refs. 22–25) have explored the use of different thermal conductivity materials to create boiling surfaces, promoting mixed boiling at high heat fluxes and consequently enhancing CHF. Recently, the concept of mixed boiling has been employed in fluid high-speed transport, where boiling with spatial symmetry breaking converts thermal energy into fluid kinetic energy.<sup>27,28</sup> In these studies, the roughness and temperature difference of the heated surface have been identified as critical factors in triggering the mixed boiling.<sup>28</sup> Inspired by the findings in Refs. 22–25, 27, and 28, can we trigger mixed boiling in three-dimensional space by incorporating extended structures on planar surfaces? This configuration is expected to improve the CHF. To explore this possibility, it is essential first to understand the mechanism of dry spot expansion on pin–fin surfaces (PFS). Figure 1(a) illustrates the configuration of the PFS, which includes both a base surface and an extended surface. At high heat flux, the surface superheat of the dry spot  $\Delta T_{\text{dry}}$  on the base surface can be approximated as follows:<sup>29</sup>

$$\Delta T_{\text{dry}} \sim R_v D_{\text{dry}}^2 q - T_{\text{sat}}, \quad (1)$$

where  $R_v$  is the effective thermal resistance of vapor,  $D_{\text{dry}}$  is the equivalent diameter of dry spot,  $q$  is total heat flux, and  $T_{\text{sat}}$  is the saturated temperature of the liquid. Equation (1) demonstrates that  $T_{\text{dry}}$  exhibits a linear relationship with  $D_{\text{dry}}$  and  $q$ . That is, given the constant heat flux,  $T_{\text{dry}}$  depends on the area of the dry spot. In the case of PFS, the temperature of the base surface ( $T_{w,b}$ ) is the key parameter to control the nucleation point density and boiling intensity on the extended surface. Of course, it also influences the temperature of the extended surface ( $T_{w,e}$ ). Therefore, the formation of dry spots on the base surface affects the boiling heat transfer of extended surface to a certain extent. In contrast, nucleate boiling on the extended surface absorbs heat from the base surface through conduction, which prevents a rise in base surface temperature and stops dry spots from spreading further. There exists an intricate interaction between the extended surface and the base surface. Especially at high heat flux, the interaction will become more intense, significantly delaying the occurrence of CHF on the boiling surface. However, as time progresses and the dry spots continue to expand, ultimately covering the whole boiling surface, steam disrupts the interference mechanism between the two boiling modes. Consequently, the boiling mode on the surface changes from mixed boiling to film boiling, and the heat transfer deteriorates.

More importantly, the uneven surface temperature distribution makes the non-hydrodynamic Burnout Effect significant, which is conducive to strengthening the mutual interference between two boiling modes at high heat flux.<sup>23,30,31</sup> This means that the temperature difference ( $\Delta T$ ) between  $T_{w,b}$  and  $T_{w,e}$  is the key factor in achieving mixed boiling mode. However, for conventional pin–fin surfaces (PFS) depicted in Fig. 1(a), increasing  $\Delta T$  is challenging due to the limited thermal resistance of the short and wide needle ribs. When the temperatures of the two surfaces are approximate in order of magnitude (e.g.,  $\Delta T \sim 1^\circ\text{C}$ ), as shown in Fig. 1(b), the dry spots on the base surface rapidly expand to the extended surface, leading to the failure of the mutual interference mechanism between nucleate boiling and film boiling. At this point, the occurrence of CHF falls within the realm of classical hydrodynamic instability theory.<sup>30,31</sup> Obviously, although PFS can trigger mixed boiling, which is unstable and

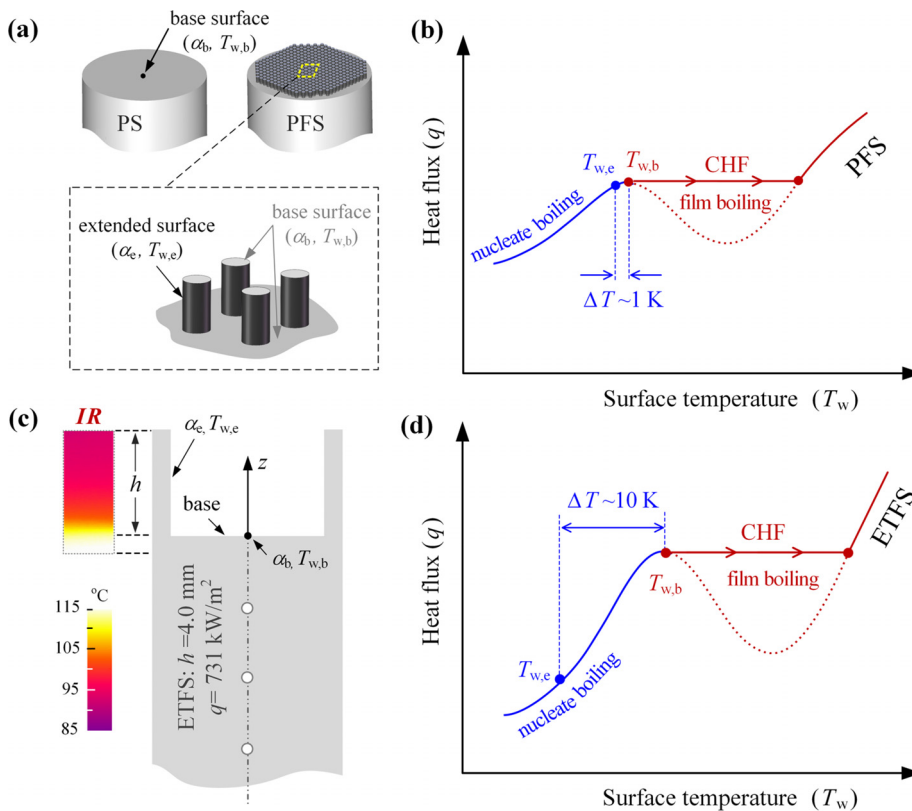


FIG. 1. Triggering mechanism of three-dimensional mixed boiling: (a) Structure of PFS, (b) boiling curve for PFS, (c) structure of ETFS, and (d) boiling curve for ETFS.

transient, improving CHF is limited. Given the above phenomena, we propose adding an extended thin film structure, instead of a pin-fin structure, on the plain surface to construct a larger  $\Delta T$ . This strategic modification aims to trigger stable three-dimensional mixed boiling and prevent the failure of mutual interference between the two boiling modes. Figure 1(c) depicts the structure of the surface with an extended thin film (ETFS), where the height of the extended film is  $h = 4.0$  mm. The temperature difference is measured using an infrared camera, corresponding to a heat flux of  $q = 731$  kW/m<sup>2</sup>. Compared to the PFS, the extended film significantly increases the non-uniformity of temperature distribution between the base and extended surfaces. As shown in Fig. 1(d), the temperature difference between the base surface and extended surface of ETFS near CHF can reach  $\Delta T \sim 10$  K. At this stage, the base surface operates in the film boiling mode with a small heat transfer coefficient  $\alpha_b$ , while the extended surface operates in the nucleate boiling mode with a larger heat transfer coefficient  $\alpha_e$ . This configuration facilitates stable mixed boiling with the mutual interaction between two boiling modes. The credit comes from the addition of the extended film structure. Another issue is the diameter of the extended film, which is subject to the limitation of Taylor wavelength  $l_{ta} = 10.877[\sigma(\rho_l - \rho_v)^{-1}g^{-1}]^{0.5} \sim 2$  cm, where  $\sigma$  is the surface tension of liquid,  $\rho_l$  is the liquid density,  $\rho_v$  is the vapor density, and  $g$  is the gravitational acceleration. Lienhard *et al.*<sup>32</sup> found that a cavity pool with a diameter approximately half of the  $l_{ta}$  provides better separation between steam and liquid, allowing for full rewetting of the surface experiencing nucleate boiling. Based on the above theories, the diameter of the extended film was ultimately determined.

### III. MATERIALS AND METHODS

#### A. Test section

Figure 2 shows the test section. Each test sample is made of a copper cylinder with an outer diameter of 10.2 mm. In Fig. 2(a), plain surface (PS), pin-fin surface (PFS), and four ETFS with the height of 2.0, 4.0, 6.0, and 8.0 mm are shown, respectively. All ETFS have an inner diameter of  $D_i = 10.0$  mm. The surface morphology characteristics are captured using an optical profiler (Bruker, ContourGT-K) with a measurement accuracy of 0.3 nm, as depicted in Fig. 2(b). From the figure, the surface is relatively smooth, with a height difference of  $5.7 \mu\text{m}$ . This type of surface exhibits hydrophilic properties ( $\beta = 10.8^\circ$ ), as indicated by a contact angle of ethanol droplets on the boiling surface. The roughness of the boiling surface, determined by extracting morphology data along the  $y = 0.045$  mm coordinate in the test area [see Fig. 2(c)], is measured to be  $Ra = 203$  nm. In the case of PFS, Fig. 2(d) shows that needle ribs have a diameter of 0.3 mm, a height of 0.5 mm, and a spacing between adjacent ones of 0.4 mm. Figure 2(e) illustrates some structural parameters of ETFS with the film height of 4.0 mm. The thickness of extended film (approximately  $\delta = 100 \mu\text{m}$ ) is obtained by measuring at ten different positions using an electron microscope. The machining error in surface fabrication is controlled within  $\pm 10 \mu\text{m}$ , rendering the effect on experimental performance negligible. The Biot number,  $Bi = \alpha\delta/\lambda \sim 10^{-3}$ , smaller than 0.1, signifies that the conduction resistance inside the body is significantly smaller than that of heat convection at the surface.<sup>33,34</sup> Thus, temperature gradients along the diameter direction inside the extended film can be considered negligible.

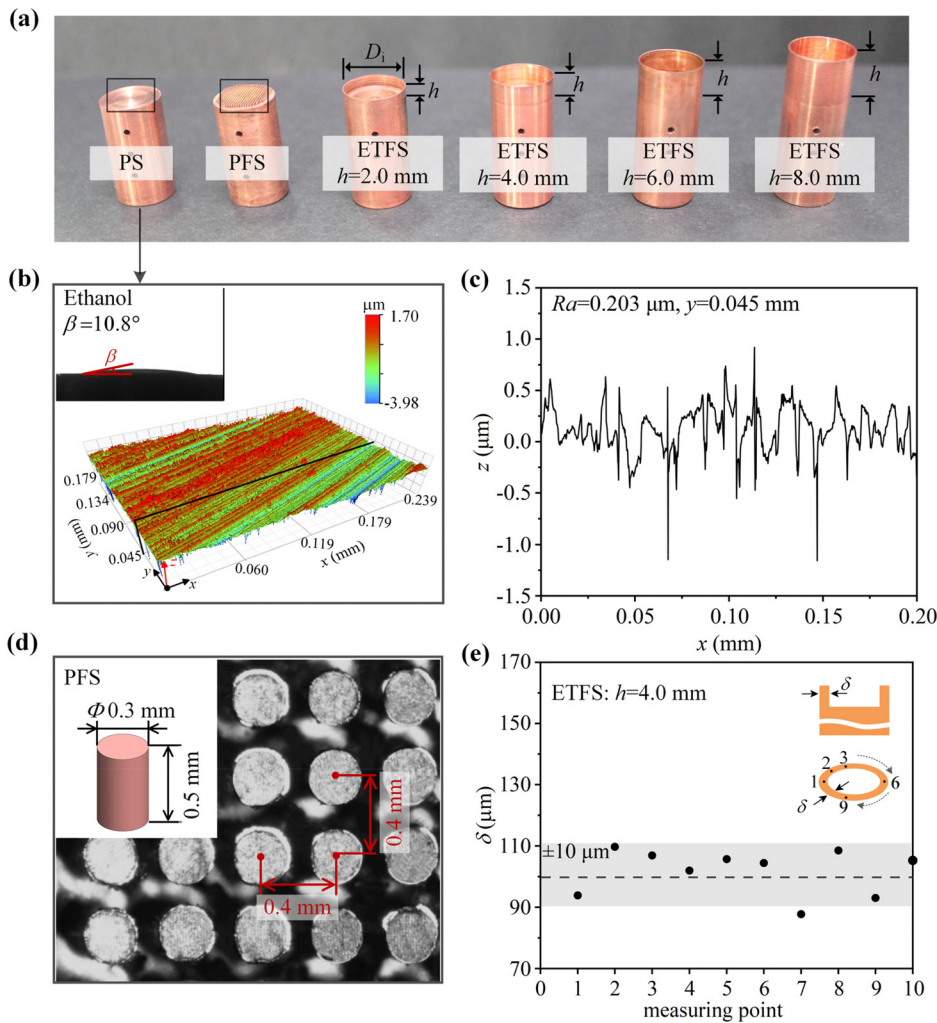


FIG. 2. Surface characterization and morphology: (a) Photographic images of PS, PFS, and ETFS surfaces; (b) and (c) scanning electron microscopy (SEM) images of PS; (d) photographic image of the pin-fin surface; and (e) thickness distribution of the extended film.

In this context,  $\alpha$  is the convective heat transfer coefficient, which is approximately  $\sim 10^4 \text{ W}/(\text{m}^2 \text{ K})$  under boiling conditions, and  $\lambda$  denotes the thermal conductivity of copper. The internal surface temperature of the extended film can be monitored using an infrared camera. In addition, each test sample has the same vertical projected area ( $78.5 \text{ mm}^2$ ). To ensure a fair comparison of heat transfer enhancement, the immersed area of PFS in ethanol is equal to that of ETFS with  $h = 4.0 \text{ mm}$ .

**B. Experimental setup**

Figure 3(a) shows the experimental setup, which is composed of a boiling pool, heating system, and data acquisition system. The boiling pool is a closed space with dimensions of  $50.0 \times 50.0 \times 10.0 \text{ mm}^3$ , constructed mainly of stainless steel and quartz glass. Its bottom center is the upper surface of the test section. At the junction of the test section and boiling pool, Teflon gaskets are used for sealing and heat insulation. There is a cover plate with a viewable window on the upper part of the boiling pool. To maintain a constant liquid level in the pool, a reflux condenser is installed above the cover plate to cool the steam and return the liquid. Additionally, four springs embedded on the top of

the cover plate are utilized to balance the internal and external pressure of the extended film, thereby preventing damage to the test section caused by uneven stress. Around boiling pool, there are four bolt columns to fasten the test section and boiling pool together. The heating system comprises a cartridge heater, auxiliary heater, and power control system. Four cartridge heaters, with a maximum heating power of 20 W each, are inserted into holes at the bottom of the test section. A voltage stabilizer, voltage transformer, and power meter jointly control the power supplied to the test section. To maintain saturated boiling, a ceramic auxiliary heater with 14 W is placed in the boiling pool, controlled by an adjustable power meter. During the boiling process, the temperatures in the test section and boiling pool are measured by K-type thermocouples with an accuracy of  $\pm 0.1 \text{ K}$  and recorded at a frequency of 20 Hz by Yokogawa DL750 data acquisition instrument. The bubble behavior was captured by a high-speed camera (Keyence, VW-9000) at the top of boiling pool, with a sampling frequency of 2000 Hz and a spatial resolution of  $4.7 \mu\text{m}$ . An infrared camera (InfrTec, ImageIR 5380) captured waves emitted from the extended film within the  $3\text{--}5 \mu\text{m}$  band through an observation window. The IR camera has

01 November 2023 08:10:57

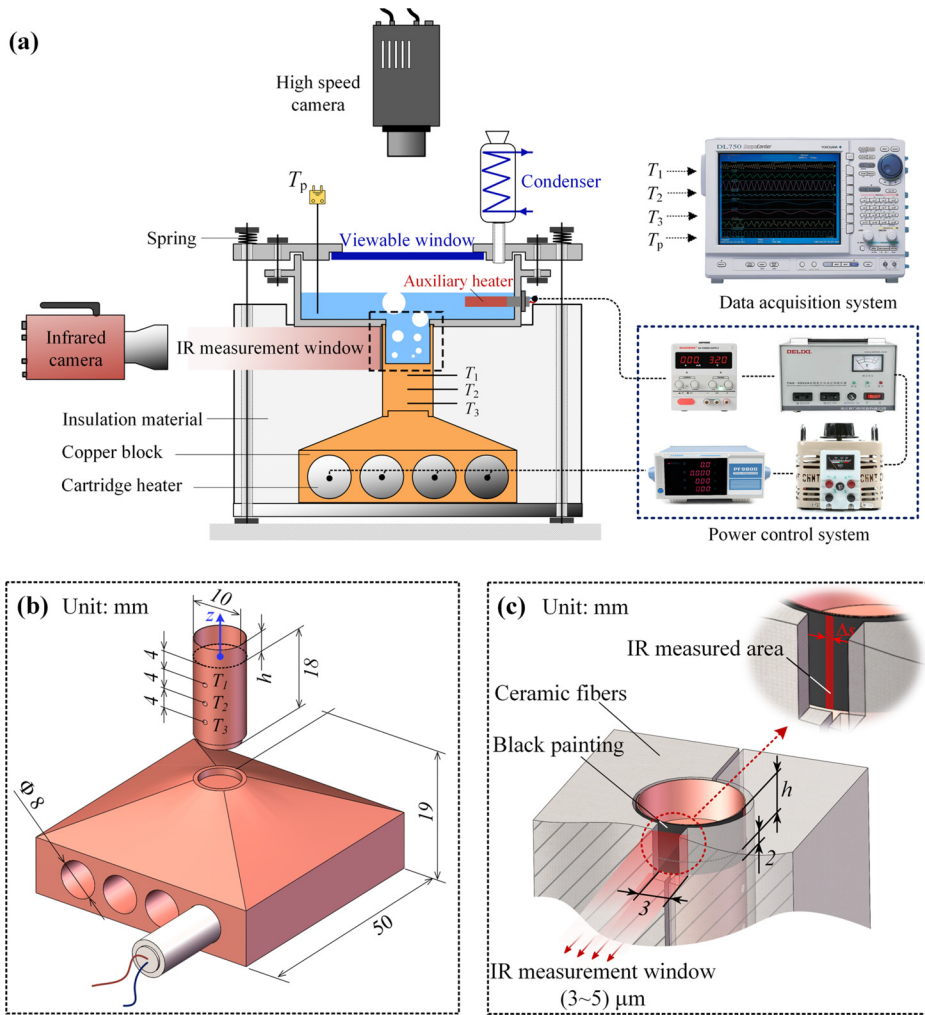


FIG. 3. Experimental setup: (a) Schematic representation of the experimental setup, (b) copper block test section (all dimensions are given in mm), and (c) measurement method of extended surface temperature by an infrared camera.

a temperature resolution of 0.02 K, operates at a sampling frequency of 200 Hz, and has a spatial resolution of 22.4 μm. All copper bodies are wrapped with ceramic fibers to minimize heat loss.

Figure 3(b) details the measurement and heating of the test section. The heating body is a copper block with a total height of 37 mm and a bottom area of 50.0 × 50.0 mm<sup>2</sup>. Four through-holes with a diameter of 8.0 mm are drilled at the bottom of heating block to accommodate cartridge heaters. Three holes, each with a diameter of 1.0 mm, spacing of 4.0 mm and depth of 5.0 mm, are present in the middle of the test section. K-type thermocouples are inserted into these holes to measure the temperatures  $T_1$ ,  $T_2$  and  $T_3$ , respectively. Figure 3(c) shows a partially enlarged view of the test section. In order

to increase the emissivity of infrared waves on the temperature measurement area, the outer surface of extended film is coated with black paint. An infrared measurement window, with a width of 3.0 mm and a height of  $h + 2.0$  mm, is positioned at the top of the ceramic fiber wrapping the test section. To eliminate the influence of surface curvature on the infrared measurements, only the surface temperature of a narrow strip area with a width of  $\Delta s = 2$  pix at the centerline is recorded.

Before each experiment, the auxiliary heater and cartridge heater are turned on to boil ethanol for two hours to eliminate dissolved non-condensable gas in the pool. The detailed physical parameters of ethanol are shown in Table I. The experiments were conducted under

TABLE I. Physical parameters of ethanol (20 °C, 101.325 kPa).

	$T_{\text{sat}}$ (°C)	$\rho$ (kg m <sup>-3</sup> )	$\lambda$ (W/m K)	$c_{p,l}$ (kJ/kg K)	$h_{fg}$ (kJ/kg)	$10^6 \times \eta_l$ (Pa s)	$10^3 \times \sigma$ (N/m)	$Pr$	$10^3 \times l_c^a$ (m)
Fluid	78.23	736.4	0.15	3.2	...	440.9	15.2	9.4	1.5
Vapor		1.65	0.02	1.72	850.0	10	...	0.861	

<sup>a</sup>Capillary length is calculated as  $l_c = (\sigma(\rho_l - \rho_v)^{-1}g^{-1})^{0.5}$ .

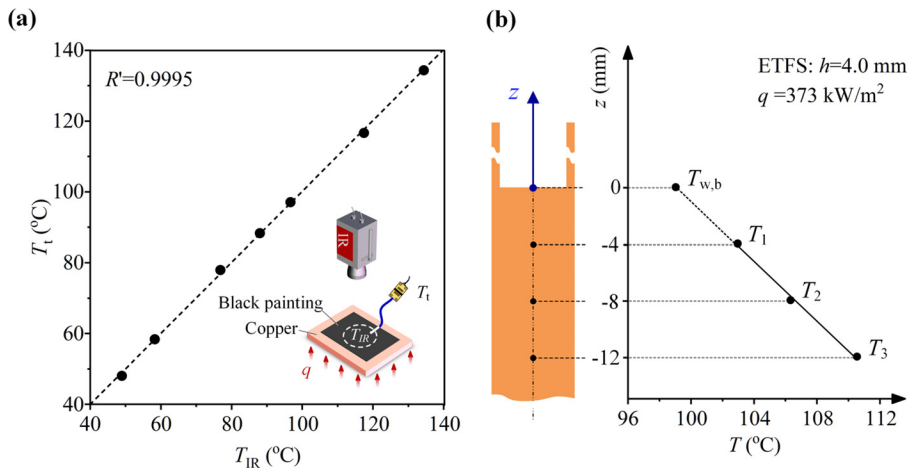


FIG. 4. Validation of the test facility: (a) Calibration of temperature measurement and (b) validation of one-dimensional heat flux during pool boiling with linear fitting.

atmospheric pressure, with an ambient temperature of  $25 \pm 0.5^\circ\text{C}$  and an ambient relative humidity of 30%. During the experiments, the ethanol level was maintained at 4.0 mm in boiling pool. Following each power increase, the temperature variations ( $T_1$ ,  $T_2$  and  $T_3$ ) are observed. Once the temperature change remains below  $1^\circ\text{C}$  within 10 min, it is deemed that the heat transfer has reached the heat balance. Subsequently, the test data are recorded using the high-speed camera, infrared camera, and Yokogawa data collector. A sudden sharp rise in boiling surface temperature indicates the occurrence of CHF. To avoid damaging the test section, the power should be turned off quickly to end the test.

### C. Data processing and the uncertainty

First of all, the infrared temperature measurement should be accurately calibrated before the experiments. As shown in Fig. 4(a), a copper plate coated with black paint is placed on the heater with an error of  $0.2^\circ\text{C}$ , and a final stable heating temperature is set for the heater. After enough time, the temperature of the copper plate is measured simultaneously by the infrared camera and thermocouple. The thermocouple is welded on the surface of copper plate to reduce contact resistance. The calibration process for the infrared camera involves correlating  $T_t$  (temperature value from thermocouple) with  $T_{IR}$  (temperature value from infrared camera). When the correlation coefficient reaches 0.995, the error between two temperature values measured by two measurement systems is very small. Since the top and outer surfaces of the extended film and copper block are well insulated, the heat transfer can be considered one-dimensional heat conduction. Hence, the total heating power ( $Q$ ), the heat dissipation of base surface ( $Q_b$ ) and the heat dissipation of extended surface ( $Q_e$ ) can be calculated according to the following equation:

$$Q = -\frac{1}{4} \pi D_o^2 \lambda \left( \frac{dT}{dz} \right)_{TC}, \quad (2)$$

$$Q_e = -\frac{1}{4} \pi (D_o^2 - D_i^2) \lambda \left( \frac{dT}{dz} \right)_{z=0,IR}, \quad (3)$$

$$Q_b = Q - Q_e, \quad (4)$$

where  $-\lambda(dT/dz)_{TC}$  is the total heat flux, and  $D_i$  and  $D_o$  are the inner and outer diameters of the extended film, respectively.  $\lambda$  is thermal

conductivity, and  $z$  is coordinated along the axis [see Fig. 4(b)]. Temperature gradient along the cylinder centerline can be approximated by  $(dT/dz)_{TC} = (3T_1 - 4T_2 + T_3)/2\Delta z$ , where  $\Delta z$  is the distance between two adjacent thermocouples. Note that  $(dT/dz)_{z=0,IR}$  is the temperature gradient at the root of extended film, which is measured with an infrared camera and calculated by the second-order upwind difference method. According to Eqs. (2)–(4), the total heat transfer coefficient  $\alpha$ , the heat transfer coefficient of extended surface  $\alpha_e$ , and the heat transfer coefficient of base surface  $\alpha_b$  can be calculated as follows:

$$\alpha = \frac{4Q}{\pi D_o^2 \Delta T_{w,b}}, \quad (5)$$

$$\alpha_e = \frac{Q_e}{\pi D_i h \Delta T_{w,e}}, \quad (6)$$

$$\alpha_b = \frac{4Q_b}{\pi D_i^2 \Delta T_{w,b}}, \quad (7)$$

where  $\Delta T_{w,b} = T_{w,b} - T_{sat}$  is the superheat of base surface, and  $T_{sat}$  is the saturation temperature of ethanol.  $T_{w,b}$  at  $z=0$  is obtained by fitting  $T_1$ ,  $T_2$  and  $T_3$  [see Fig. 4(b)].  $\Delta T_{w,e}$  is the average superheat of extended surface, and extended surface temperature is  $T_{w,e} = \int_0^h T dz/h$ . Integrating Eqs. (4)–(7), the total heat transfer coefficient is rewritten as follows:

$$\alpha = \alpha_b \left( \frac{D_i}{D_o} \right)^2 + \alpha_e \frac{4D_i h \Delta T_{w,e}}{D_o^2 \Delta T_{w,b}} \approx \alpha_b + \alpha_e \frac{4h \Delta T_{w,e}}{D_o \Delta T_{w,b}}. \quad (8)$$

Due to the coupling of heat transfer between the extended surface and base surface, a new ratio factor ( $RF_z$ ) is introduced to further explore the competitive relationship between two heat transfer surfaces in enhancing heat transfer performance,

$$RF_z = \frac{\alpha - \alpha_b}{\alpha_b} = \frac{4h}{D_o} \times \frac{\alpha_e}{\alpha_b} \times \frac{\Delta T_{w,e}}{\Delta T_{w,b}}. \quad (9)$$

$RF_z$  depends on the aspect ratio ( $h/D_o$ ), the ratio of heat transfer coefficient between extended surface and base surface ( $\alpha_e/\alpha_b$ ), and the superheat ratio of two surfaces ( $\Delta T_{w,e}/\Delta T_{w,b}$ ). By integrating Eqs. (5), (6), (8) and (9), the contribution of the extended surface to heat dissipation is

$$\frac{Q_e}{Q} = \frac{RF_x}{1 + RF_x}, \tag{10}$$

and it is a function of  $RF_x$ . In this way, the heat dissipation  $Q_b$  and  $Q_e$  is finally decoupled. Following the error propagation criterion,<sup>35</sup> the maximum uncertainty of heat flux and heat transfer coefficient is 4.8% and 4.5%, respectively.

#### IV. RESULTS AND DISCUSSION

##### A. Heat transfer performance

First, to verify the reliability of our experiment, the boiling curve obtained from PS was compared with the prediction results of the classical Rohsenow equation<sup>36</sup>

$$q = \eta_l h_{fg} \left[ \frac{g(\rho_l - \rho_v)}{\sigma} \right]^{1/2} \left( \frac{c_{p,l} \Delta T_{sat}}{C_{s,l} h_{fg} Pr_l^n} \right)^3, \tag{11}$$

where  $c_{p,l}$  is specific heat of liquid,  $h_{fg}$  is latent heat of vaporization,  $\eta_l$  is dynamic viscosity of liquid, and  $Pr_l$  is Prandtl number of liquid. Constants  $C_{s,l} = 7.9 \times 10^4$  and  $n = 2.3$  are related to the surface-liquid combination.<sup>36</sup> According to Eq. (11), the predicted CHF of PS is 275 kW/m<sup>2</sup>. Note that this value applies only to heating surfaces with large areas. In cases where the characteristic size ( $L$ ) of the heating surface is smaller than the critical value of 5 cm (our current heating surface has  $L = 1$  cm), the size effect causes an increase in the boiling critical heat flux  $q_{CHF}$ .<sup>37</sup> Referring to the experimental curve provided by Raieny and You,<sup>38</sup> which establishes a relationship between the critical heat flux and the size of the heating surface, we can obtain the predicted CHF is 347 kW/m<sup>2</sup> for saturated pool boiling on PS (according to  $q_{CHF,small}/q_{CHF,large}$  where  $q_{CHF,small}$  and  $q_{CHF,large}$  represent the critical heat flux under small and large heating surfaces, respectively). Our measured CHF is 354 kW/m<sup>2</sup>, which is 2% higher than that. Hence, considering the size effect of the heating surface, our experimental results are reasonable.

Figure 5 shows the boiling curves of each test surface (PS, PFS, and ETFS). It can be observed that the boiling curves of the structured surfaces (ETFS and PFS) shift to the left compared to that of the plain surface (PS), which is consistent with findings reported in Refs. 39 and

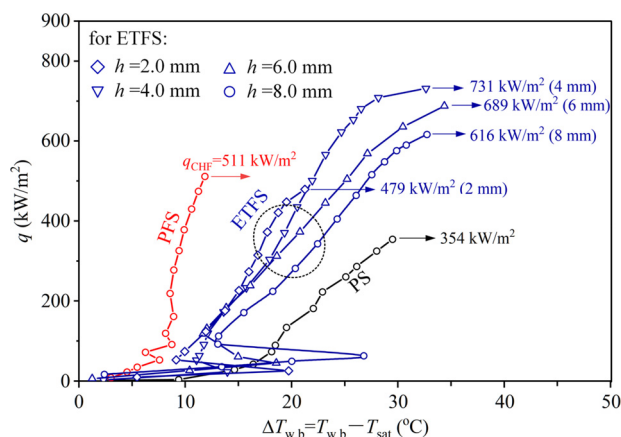


FIG. 5. Boiling curves for test surfaces with different structures. The arrows indicate the critical heat flux (CHF) corresponding to each curve.

40. At low heat flux, the heat transfer performance of PFS and ETFS is improved due to the increased surface area provided by the extended structures. However, at high heat flux, the enhancement mechanism of boiling heat transfer becomes more complex for structured surfaces, involving complex vapor-liquid phase separation process. In Fig. 5, the boiling curve of PFS appears nearly vertical, indicating a high sensitivity of the boiling surface to wall superheat. That is, the heat transfer coefficient of PFS is large. However, PFS is prone to be covered by a gas film at high heat flux, having a CHF of 511 kW/m<sup>2</sup> approximately. For ETFS, although the superheat is slightly higher than that of PFS under the same heat flux, it shows significant potential in improving CHF. This is also a highlight of three-dimensional mixed boiling brought by innovative structures. The maximum CHF of ETFS is 731 kW/m<sup>2</sup>, which is about 45% and 110% higher than that of PFS and PS, respectively.

Furthermore, Fig. 5 also presents the differences in boiling curves for ETFS with different heights. The height of extended film is a key parameter influencing the boiling dynamics. For ETFS with a height of 2.0 mm, the CHF value is  $q_{CHF} = 479$  kW/m<sup>2</sup>, and the boiling curve is closer to that of PFS. With an increase in height, the CHF significantly increases. In the range of film heights from 2.0 to 8.0 mm, there exists an optimal height of 4.0 mm make the entire boiling surface have the best heat transfer performance. This phenomenon was also observed by Rainey and You<sup>41</sup> in their experiments on pin-fin surfaces with millimeter-scale heights. However, the boiling mechanisms of the two structural surfaces are different. In our experiment, the upward heat transfer along the film is reduced due to the thinner extended film (100 μm). Consequently, for ETFS, the direct cooling of the base surface by the main liquid flow (at the top of the structure) has a less pronounced effect on the CHF. In fact, this is related to the change in boiling dynamics within the pool. When periodic flooding occurs in the pool due to the instability of the gas-liquid channel, the higher extended film increases the resistance and reduces the frequency for cold liquid reflux, thus preventing adequate wetting of the heating surface and ultimately leading to a boiling crisis.<sup>42,43</sup> Further explanation will be provided in Secs. IV B-IV D.

##### B. Boiling phenomenon

To differentiate the boiling process and mechanism between ETFS and PFS, the boiling process on PFS was first described. For ethanol liquid on the surface, the thickness of thermal boundary layer is about 100 μm, estimated by  $\delta_T = 3.22 \lambda_l / \alpha$ ,<sup>44</sup> having the same order as the height of the needle rib. Here,  $\lambda_l$  is the thermal conductivity of ethanol. Therefore, the extended surface of the needle rib and the base surface is considered to have approximately the same temperature and heat transfer coefficient, namely,  $T_{w,e} \sim T_{w,b}$ , and  $\alpha_b \sim \alpha_e$ .<sup>43,45,46</sup> This determines that the two surfaces have the same boiling mode. Figure 6 shows the concept diagram of boiling process under low, medium and high heat flux. When  $q$  and  $\Delta T_{w,b}$  are very small, the thermal conditions are approximately the same for extended and base surfaces, which is conducive to increasing the nucleation density. Nucleate boiling allows more heat to be dissipated from the heating surface in latent heat [see Fig. 6(a)]. With increasing  $q$ , the bubbles in the needle rib gap converge in the horizontal and vertical directions, respectively [see Fig. 6(b)]. That is to say, under medium heat flux conditions, slightly increased surface temperature ( $\delta'$ ) may cause bubbles to rapidly fill the needle rib gap. At this stage, liquid is replenished to



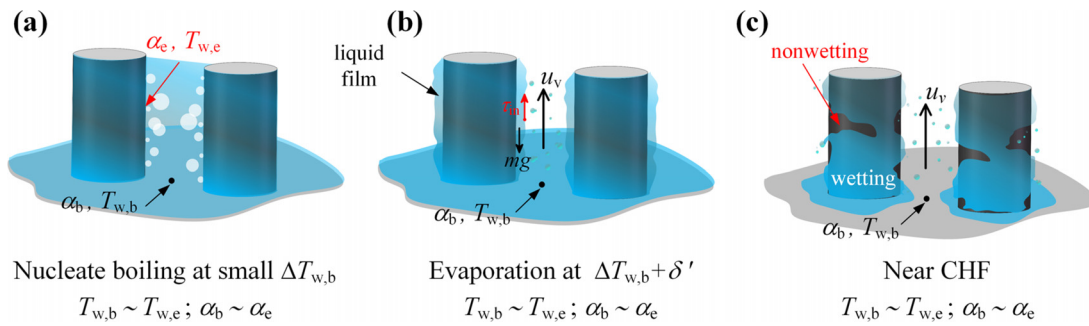


**FIG. 6.** Schematic illustrations of pool boiling on a pin-fin surface. (a) Low heat flux regime, (b) moderate heat flux regime, and (c) high heat flux regime near the critical heat flux (CHF).

the base surface along the surface of needle rib due to the capillary force and self-gravity. The rapid evaporation of liquid film results in a lower surface superheat for PFS compared to ETFS.<sup>44,47</sup> However [see Fig. 6(c)], once the bubbles between the ribs and at the top of the needle aggregate, a large steam blanket will cover the boiling surface, and the resistance of liquid replenishment located under the steam blanket will significantly increase in both vertical and horizontal directions.<sup>41,48</sup> Subsequently, the huge shear force generated by steam scouring began to tear the liquid film on the surface of needle rib, resulting in the non-wetting zone on the surface of needle rib [see Fig. 6(c)], and finally triggering CHF.

Conversely, the boiling mechanism of ETFS is different from that of PFS. Taking a sample of ETFS with a height of 4.0 mm as an example. Figure 7 shows three stages of the boiling process on ETFS, corresponding to three boiling modes: nuclear boiling/convection (NB/C), partial film boiling/nuclear boiling (PFB/NB), and film boiling/nuclear boiling (FB/NB) (the terms front and rear the “/” symbol represent the heat transfer mode of the base surface and extended surface, respectively). The figure also includes high-speed photography images capturing the boiling phenomena at a specific heat flux in different stages. For ethanol under atmospheric conditions, the bubble detachment diameter  $D_b$  is approximately 0.3 mm, estimated from the equation  $D_b = 0.0208\beta l_c$ ,<sup>49</sup> where  $l_c = 1.5$  mm is the length of ethanol capillary, and  $\beta$  is obtained from measurement, approximately 33 times the diameter of the cavity pool. Therefore, in the first boiling stage, the active nucleation points and bubbles in the cavity are independent of each other, and the mainstream liquid adequately wet the base surface. For instance, at  $q = 173$  kW/m<sup>2</sup> and  $\Delta T_{w,b} = 13.6$  °C, whether at  $t = 0$  or 100 ms, the cavity pool is filled with isolated bubbles, and there is no bubble aggregation. Due to the low temperature of extended surface in this stage, convective heat transfer is the main process occurring on the surface. Therefore, we call it the nuclear boiling/convection (NB/C) heat transfer mode.

With increasing heat flux, boiling enters the second stage. More nucleation points and larger bubbles detached from the cavity, resulting in mutual interference and lateral aggregation among isolated bubbles. The newly merged bubbles exhibit greater buoyancy and ascend at an increased rate. Seeing boiling visualization of the second stage ( $q = 501$  kW/m<sup>2</sup>) in Fig. 7, it shows that the liquid flowing back to the bottom of bubble, surrounds the bubble and continues to scour the root of the bubble ( $t = 0-4$  ms). At this time, the frequency of bubble detachment in the form of neck contraction manner increases. After the bubbles detach, a residual small bubble is left on the surface and

gradually shrinks with condensation caused by supplemental liquid. Similar bubble detachment processes have also been reported by Chu *et al.*<sup>50</sup> When the replenished liquid becomes overheated again, the boiling behavior repeats. Recently, Li *et al.*<sup>51</sup> also reported this process on a heated platinum wire, where the neck forms at the root of the vapor film due to the influence of the Marangoni force. The visualization shows the presence of dry spots underneath the coalesced large bubbles ( $t = 127$  ms). Initially, these dry spots contract during the bubble detachment processes and then expand as the remaining bubbles grow. Consequently, the appearance of dry spots is intermittent. This boiling mode is called partial film/nuclear boiling, abbreviated as PFB/NB. In this stage, the transition from nuclear boiling to film boiling begins on the base surface, and some extended surfaces begin to undergo nuclear boiling due to the increase in temperature.

When the heat flux is sufficiently high, boiling enters its third stage. In this stage, the temperature of the dry spot increases over time, causing more liquid to evaporate on the area adjacent to the dry spot area. As a result, intermittent dry spots disappear and irreversible dry spots begin to appear. Generally, when stable dry spots cover a significant portion of the heating surface, the boiling process usually becomes uncontrollable, and the soaring surface temperature can cause damage to the test piece, leading to a boiling crisis.<sup>52,53</sup> In the present study, however, we found a new boiling phenomenon on ETFS at high heat flux. As shown in the III stage of Fig. 7, when  $q = 731$  kW/m<sup>2</sup> is applied to the surface (resulting in  $\Delta T_{w,b} = 32.7$  °C), a dry spot with an approximate equivalent diameter of 5.0 mm persists beneath the elongated bubble warhead, indicating the onset of a stable film boiling state ( $t = 0-121$  ms). During the period ( $t = 47-76$  ms), bubble growth behavior was observed on the extended surface. The boiling mode of this stage is named film boiling/nuclear boiling (FB/NB), denoting the occurrence of film boiling on the base surfaces and nuclear boiling on the extended surfaces, respectively.

To gain further insights into the boiling mechanism on ETFS, the temperature fluctuation characteristics at the root of the extended film can be analyzed using the standard deviation of temperature ( $\sigma_T$ ). It is calculated using the following equation:

$$\sigma_T = \sqrt{\frac{1}{n} \sum_{i=1}^n (T_{e,r} - \bar{T}_{e,r})^2}, \quad (12)$$

where  $T_{e,r}$  is temperature at the root of extended film, which is obtained by an infrared camera.  $\bar{T}_{e,r}$  is average temperature,  $n$  is the

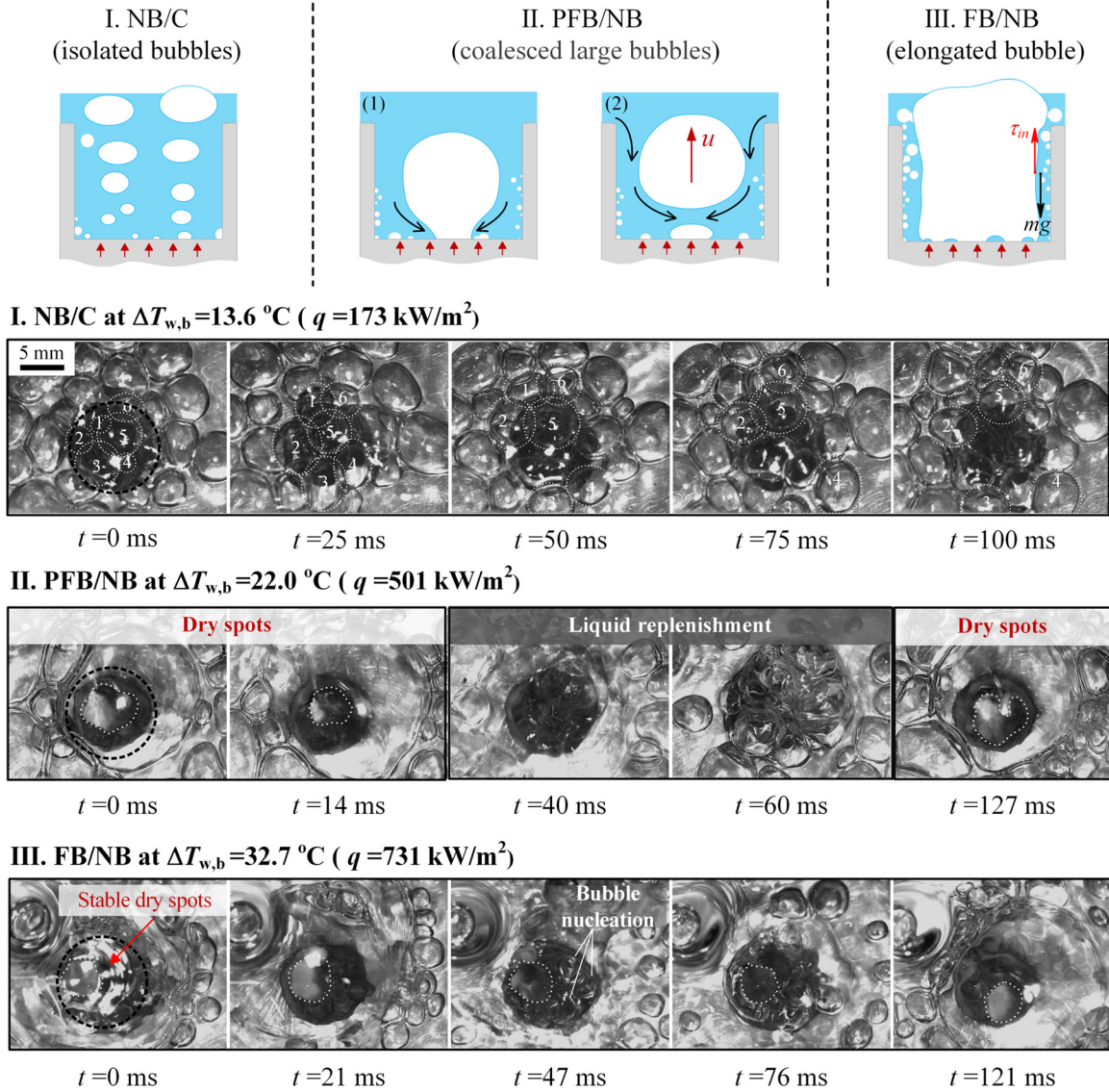


**FIG. 7.** Three stages of the boiling process on ETFS, corresponding to three distinct boiling modes: nuclear boiling/convection (NB/C), partial film boiling/nuclear boiling (PFB/NB), and film boiling/nuclear boiling (FB/NB).

amount of data collected. From a physical perspective, the larger the value of  $\sigma_T$ , the stronger the surface temperature fluctuation. Figure 8 shows the transition from NB/C to PFB/NB, then to FB/NB mode, and presents three linear variation laws (the lines are drawn in black, blue, and red colors, which correspond to each of the three boiling modes). For the initial stage at low heat flux, active nucleation points are uniformly distributed on base surface, and bubbles can continuously detach from base surface. At this time, the temperature of the boiling surface is stable, as indicated by  $\sigma_T = 0.08$  at the test point. When  $\Delta T_{w,b}$  exceeds  $15.5\text{ }^{\circ}\text{C}$ , the temperature starts to oscillate, signifying the transition from the stable NB/C mode to the unstable PFB/NB mode in the pool. This oscillation is caused by the contraction and expansion behavior of dry spots at the bottom of the pool, as discussed in Fig. 7.

Specifically, the surface temperature increases as the dry spots expand and decrease as that contract. With a further increase in  $\Delta T_{w,b}$ , the temperature fluctuation at the measurement point intensifies. In this stage,  $\Delta T_{w,b}$  ranges from  $15.5\text{ }^{\circ}\text{C}$  to  $26.5\text{ }^{\circ}\text{C}$ , and  $\sigma_T$  ranges from 0.08 to 0.56. After that, the FB/NB boiling mode began, and the  $\sigma_T$  curve almost flattened with a maximum increase of 0.08, which continued until reaching CHF. During this stage, the temperature of the base surface undergoes violent oscillations.

However, as shown in the FB/NB stage in Fig. 7, the periodic expansion and contraction of dry spots on the base surface have ended, and a large area of base surface remains dry for a long time. Thus, the temperature oscillation at the test point primarily originates from the interior of the falling liquid film on extended surface.

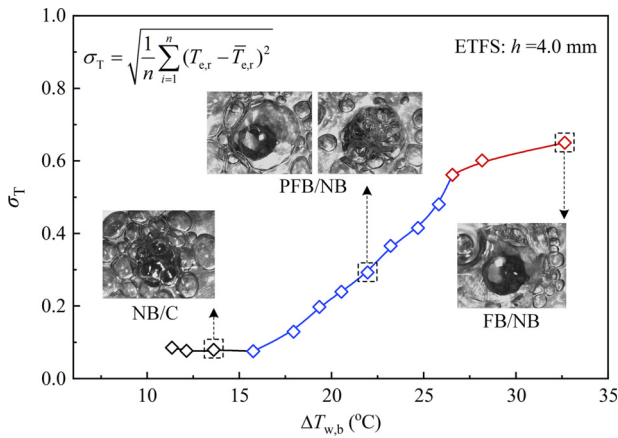


FIG. 8. Temperature standard deviation  $\sigma_T$  of the base surface in three boiling modes: NB/C, PFB/NB, and FB/NB.

Specifically, due to the heat conductivity of the liquid film at the bottom of bubble, the bubble can continue to grow after being swept away from the nucleation point by the falling liquid on the extended surface. Part of the bubbles overflow out of the liquid film and rupture, increasing disturbance of liquid film and causing temporary rupture of the liquid film on extended surface, ultimately resulting in surface temperature fluctuations. Similar secondary nucleation behavior in superheated falling liquid film has also been observed by El-Genk and Saber.<sup>54</sup> In fact, the presence of large dry spots increases the temperature of the base surface, which, in turn, accelerates nucleation and boiling within the liquid film on the extended surface. Overall, by incorporating an extended film structure onto the plain surface, a spatially non-uniform temperature distribution can be generated, triggering three-dimensional mixed boiling comprising nuclear boiling and film boiling. The mutual interference between these modes in different regions effectively inhibits the deterioration of heat transfer caused by the deactivation of a large area of nucleation sites on the boiling surface, thereby delaying the occurrence of CHF.

C. Effect of extended film height

The height of the extended film plays a crucial role in the interaction between nuclear boiling and film boiling on both boiling surfaces, which significantly impacts heat transfer performance and boiling behavior. From Eq. (12), the standard deviation ( $\sigma_T$ ) of temperature ( $T_{e,r}$ ) at the root of extended surface can be obtained under near-CHF conditions. Figure 9 illustrates the regularity of  $\sigma_T$  for ETFS with film heights of 2.0, 4.0, 6.0, and 8.0 mm, and compares it with that of PS and PFS. Notably, a substantial synergistic relationship between critical heat flux and temperature oscillation behavior, especially for ETFS structures, is observed. Among all the surfaces, ETFS with  $h = 4.0$  mm exhibits the strongest temperature oscillations, characterized by a maximum standard deviation of  $\sigma_T = 0.65$ . This behavior is visually evident in the illustration (see Fig. 9), with temperature oscillating within a range of  $\pm 1.6^\circ\text{C}$  around the average value ( $\bar{T}_{e,r}$ ). However, decreasing or increasing  $h$  would weaken temperature oscillation. For ETFS with  $h = 2.0$  and  $8.0$  mm,  $\sigma_T$  decreases to 0.24 and 0.40, respectively. In comparison, the surface temperatures of PS and PFS remain

relatively stable, with  $\sigma_T$  values of 0.03 and 0.07, respectively. These findings indicates that the CHF enhancement is accompanied by a decrease in surface temperature stability for ETFS, signifying a distinct heat transfer mechanism compared to that of PS and PFS.

Previous studies have shown that nucleate boiling on the region adjacent to the dry spot is crucial to maintaining temperature stability at high heat flux.<sup>31,50,52,55,56</sup> Figure 10(a) illustrates the boiling behavior on PS. Due to the substantial difference in heat transfer coefficients between the dry spot region at the bottom of the bubble and the nucleate boiling region at the edge of the bubble, a significant temperature gradient exists in the horizontal direction of the base surface. It facilitates lateral heat transport, preventing the occurrence of temperature jumps resulting from heat accumulation on the dry spot area. However, with heat flux near CHF, the merger of adjacent dry points accelerates the diffusion of three-phase contact lines. When the energy barrier at the interface fails to impede this diffusion, a vapor blanket forms over the heating surface, initiating film boiling ( $\Delta T_{w,b} = 29.5^\circ\text{C}$ ,  $q_{CHF} = 354 \text{ kW/m}^2$ ). In the case of ETFS [see Fig. 10(b)], the extended film structure not only restricts excessive expansion of the three-phase contact line but also increases the temperature difference between the two boiling regions: nucleate boiling on the extended film surface and film boiling on the base surface. This configuration effectively delays the overall evolution of boiling instability caused by dry spots and prevents the weakening or failure of boiling interference.

Figure 10(c) presents the time-averaged temperature distribution of the test sample at  $q \approx q_{CHF}$ , which aids in identifying the boiling behavior on ETFS with different heights. The  $z$ -coordinate originates from the center of the base surface and is oriented vertically upward from the base surface [see Fig. 10(b)]. The temperature of the extended surface portion ( $z \geq 0$ ) is captured by an infrared camera, while the temperature of the base surface portion ( $z \leq 0$ ) is measured by thermocouples. The difference  $\Delta T$  between  $T_{w,e}$  and  $T_{w,b}$  is a key parameter that influences the boiling mode in the pool and is affected by the height of extended film. That is,  $\Delta T$  decreases with decreasing  $h$ . Notably, near CHF, the  $\Delta T = 4.4^\circ\text{C}$  of ETFS with  $h = 2.0$  mm is much lower than that of an ETFS with  $h = 4.0$  mm,  $h = 6.0$  mm and  $h = 8.0$  mm. As discussed in Sec. II, low temperature differences tend to converge the boiling modes of the two surfaces, making it difficult to maintain mixed boiling in the pool, which is not conducive to

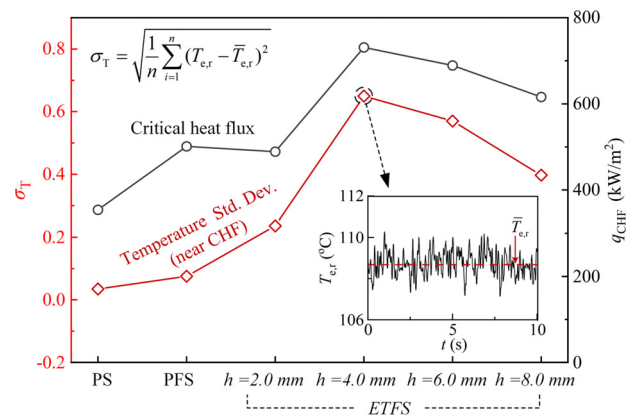
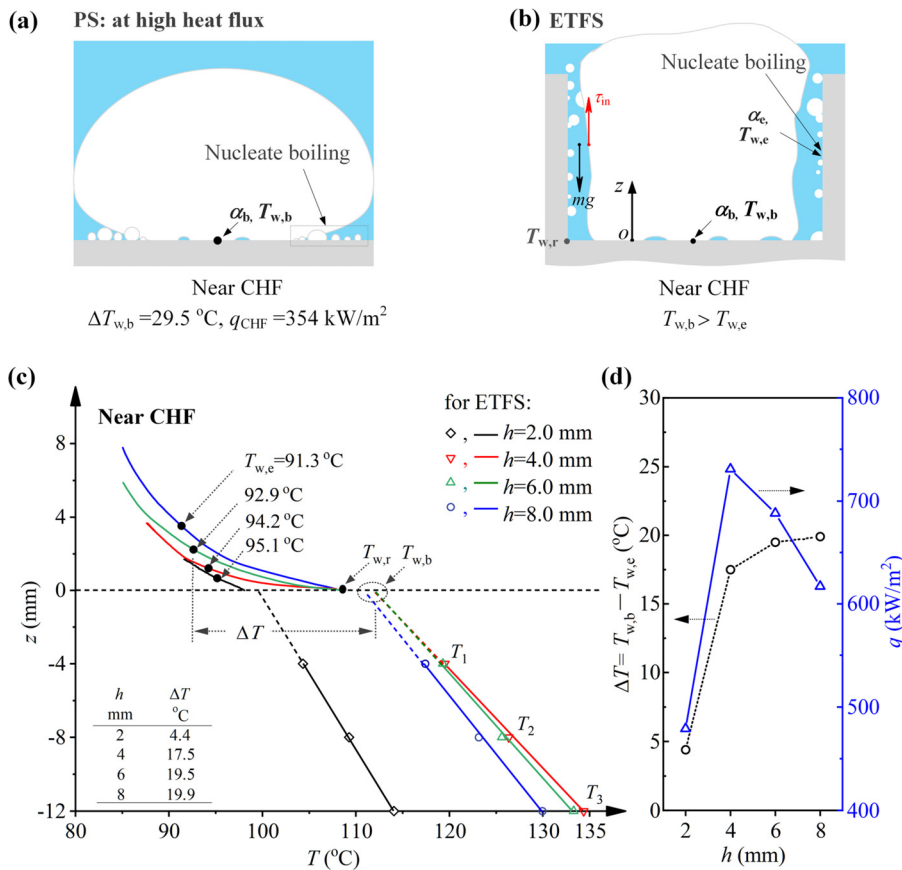


FIG. 9. Comparison of temperature standard deviation  $\sigma_T$  for PS, PFS, and ETFS with extended heights of 2.0, 4.0, 6.0, and 8.0 mm.



**FIG. 10.** Mechanism of CHF Enhancement: (a) Coexistence of nuclear boiling and dry spot on the plain surface, (b) nuclear boiling in the falling liquid film stabilizes the base surface temperature, (c) temperature distribution and difference on ETFS with varying heights, and (d) temperature difference between the base surface and extended surface, along with corresponding CHF at different heights.

further enhancing CHF. At high heat flux, for ETFS with  $h = 2.0\text{ mm}$ , the spatial confinement is minimal, and the bubble detachment diameter is large, resulting in the periodic detachment of bubbles from the boiling surface in a quasi-spherical shape.<sup>57</sup> At this time, referring to Fig. 8,  $\sigma_T = 0.24$ , indicating that the boiling process is in the PFB/NB mode, where the periodic detachment of bubbles in the pool may dominate the boiling process.

However, the extended surface with higher height contributes to a larger temperature difference, which promotes the dominance of mixed boiling in the boiling behavior at high heat flux. As shown in Fig. 10(c), the  $\Delta T$  of ETFS with  $h = 4.0\text{ mm}$  and  $h = 6.0\text{ mm}$  is  $17.5\text{ }^\circ\text{C}$  and  $19.5\text{ }^\circ\text{C}$ , respectively. Figure 10(d) demonstrates a significant increase in CHF for ETFS with  $h = 4.0\text{ mm}$  compared to other tested samples, reaching a value of  $731\text{ kW/m}^2$ . The specific analysis is as follows: As discussed in Sec. IV C, mixed boiling (FB/NB) induces severe temperature fluctuations in the pool. With a further increase in  $h$ , such as  $h = 8.0\text{ mm}$ , a sharp increase in vapor release resistance may hinder and delay the entry of liquid into the pool, leading to partial surface dryout, thus weakening the mutual interference effect of mixed boiling. Additionally, an increasing  $h$  also causes an increase in its vertical thermal resistance, reducing the impact of heat dissipation from the top of extended surface, although there may be liquid film evaporation there. In summary, the influence of the extended film height on CHF mainly stems from the mutual

interference between nucleate boiling and film boiling in mixed boiling. As  $h = 4.0\text{ mm}$ , ETFS achieves the optimal height and has the largest CHF.

**D. Role and contribution of extended surface**

According to Eqs. (5)–(10) in Sec. III C, we quantitatively decoupled the role of extended film in the boiling interference process [see Fig. 11]. Figure 11(a) shows the variation of ratio factor  $RF_z$  with  $\Delta T_{w,b}$ . The  $RF_z$  represents the competitive relationship between the extended surface and the base surface in enhancing heat transfer performance. It depends on three key parameters: the height of the extended surface  $h$ , the heat transfer coefficient ratio between the extended surface and base surface ( $\alpha_e/\alpha_b$ ), and the superheat ratio between the two surfaces ( $\Delta T_{w,e}/\Delta T_{w,b}$ ). The curves of  $\alpha_e/\alpha_b$  and  $\Delta T_{w,e}/\Delta T_{w,b}$  are presented in Figs. 11(b) and 11(c), respectively. Comparing Figs. 11(a)–11(c), it can be observed that the curve of  $\alpha_e/\alpha_b$  exhibits a similar trend to that of  $RF_z$ , with a more pronounced effect observed at  $h = 4.0\text{ mm}$ . Both of them exhibit a highly sensitive characteristic to  $\Delta T_{w,b}$ . However, as shown in Fig. 11(c), when  $\Delta T_{w,b} > 25\text{ }^\circ\text{C}$ , the effect of  $h$  on  $\Delta T_{w,e}/\Delta T_{w,b}$  becomes fragile. In fact,  $\Delta T_{w,e}/\Delta T_{w,b}$  is associated with cooling effects originating from the tip of the extended film, and significant cooling effects will reduce  $\Delta T_{w,e}/\Delta T_{w,b}$ .<sup>39,58</sup> Thus,  $h$  and  $\alpha_e/\alpha_b$  dominate the competition between the base surface and extended surface. This finding

01 November 2023 08:10:57

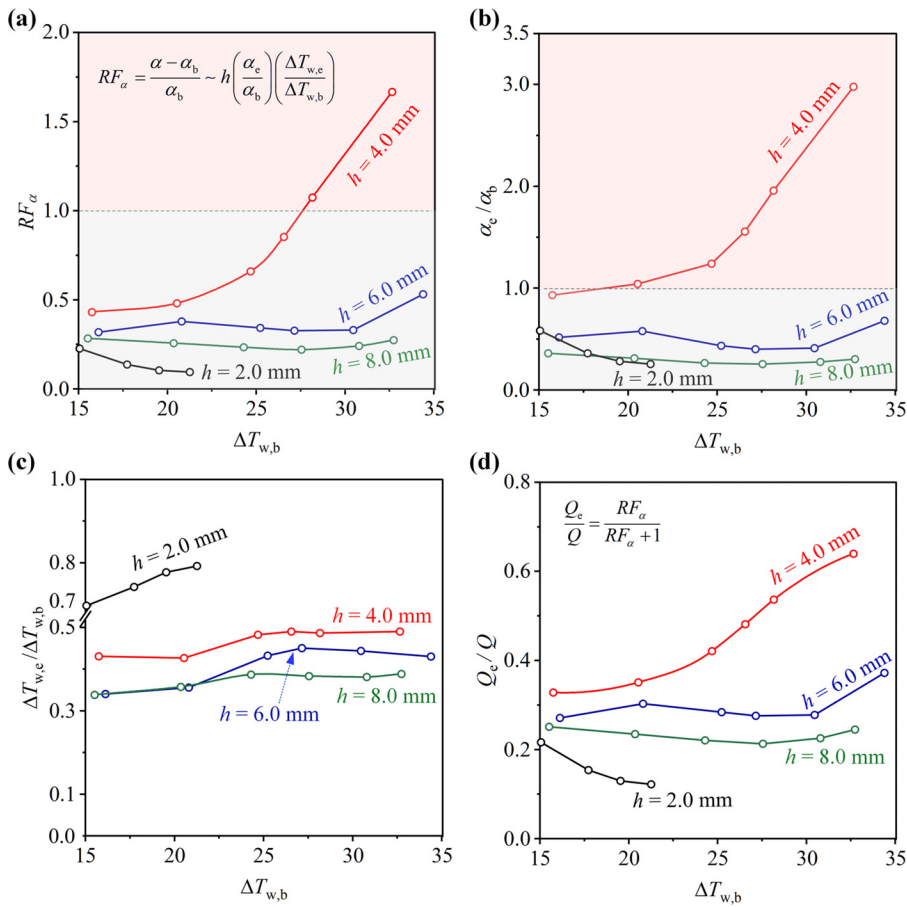


FIG. 11. Role and contribution of extended surface to heat dissipation under varying  $\Delta T_{w,b}$  and  $h$ : (a) For  $RF_\alpha$  (b) for  $\alpha_e/\alpha_b$ , (c) for  $\Delta T_{w,e}/\Delta T_{w,b}$ , and (d) for  $Q_e/Q$ .

supports the assumption presented in Sec. IV C, which posits that the top cooling effect of the extended surface has a negligible impact on CHF for ETFS.

As the base surface overheats, the influence of  $h$  on  $\alpha_e/\alpha_b$  becomes more pronounced. Among the four cases of extended height,  $\alpha_e/\alpha_b$  for  $h = 4$  mm exhibits the highest sensitivity to the base surface temperature. Specifically, when  $\Delta T_{w,b} = 25.5^\circ\text{C}$ , a sudden rise in the  $\alpha_e/\alpha_b$  curve is observed for ETFS with  $h = 4.0$  mm. This change is attributed to the beginning of film boiling/nuclear boiling (FB/NB), which is confirmed by an approximate inflection temperature that occurs during the transition from partial film boiling/nuclear boiling (PFB/NB) to FB/NB on the  $\sigma_T - \Delta T_{w,b}$  curve. Near the critical heat flux (CHF),  $\alpha_e/\alpha_b \approx 3$ , indicates the dominant boiling-enhanced mechanism of extended surfaces. However, this enhancement degrades as the height of the extended surface increases or decreases. As shown in Fig. 11(b), for  $h = 2.0, 6.0,$  and  $8.0$  mm,  $\alpha_e/\alpha_b$  remains consistently below 1.0 at all levels of overheating ( $\Delta T_{w,b}$ ). In fact, the ETFS with  $h = 2.0$  mm does not exhibit significant spatial effects as it reduces the temperature difference between the base surface and extended surface. Therefore, in the case of  $h = 2.0$  mm,  $\alpha_e/\alpha_b$  decreases with the increase in  $\Delta T_{w,b}$  [see Fig. 11(b)]. Note that, the plain surface (PS) represents a special case of ETFS with  $h = 0$  mm. For a detailed discussion, refer to Sec. IV C. On the other hand, as higher extended film heights are employed, the  $\alpha_e/\alpha_b$  curve tends to flatten. This implies that the

enhanced spatial effect weakens the strengthening effect of the extended surface on boiling heat transfer. Further increase  $h$ , for example,  $h > 8$  mm, result in the disappearance of mixed boiling, and boiling is primarily dominated by flooding dynamics,<sup>59</sup> which falls beyond the scope of this study.

Finally, the contribution of the extended surface to the boiling heat transfer is shown in Fig. 11(d), represented by the ratio of the heat transfer amount ( $Q_e$ ) from the extended surface to the total heat transfer ( $Q$ ). Obviously,  $Q_e/Q$  is a function of  $RF_\alpha$ . Hence, the influence of  $\Delta T_{w,b}$  and  $h$  on  $Q_e/Q$  aligns with their impact on  $RF_\alpha$ . Specifically, for ETFS with  $h = 2.0, 4.0, 6.0$  and  $8.0$  mm, the contribution values of the extended surface to boiling heat transfer at near CHF are 12%, 64%, 37% and 24%, respectively. These results further confirm that the optimal height for the extended film surface in this study is  $h = 4.0$  mm, as it exhibits the highest contribution ( $Q_e/Q = 64\%$ ) to boiling heat transfer.

For array structures with multiple ETFS units, there exist interactions not only between the extended surface and base surface of each ETFS unit but also between adjacent ETFS units, resulting in flow disturbances and variations in temperature distribution. Therefore, mixed boiling can be triggered more easily by manipulating the temperature difference between the extended surface and the base surface, and such temperature difference can be controlled by adjusting the ratio of the thickness to height of the extended surface.

## V. CONCLUSIONS

Based on the concept of mixed boiling, a novel boiling surface was constructed by adding an extended thin film on the plain surface, realizing the coexistence of nucleate boiling and film boiling modes in three-dimensional space. The pool boiling heat transfer on plain surfaces (PS), pin-fin surfaces (PFS), and surfaces with extended thin film (ETFS) were studied experimentally using high-speed cameras and infrared visualization. The contribution of the extended surfaces to boiling heat transfer was decoupled and analyzed. The main research results are summarized as follows:

- (1) Compared to PS and PFS, ETFS exhibits a significant enhancement in CHF, with the maximum enhancement in CHF by approximately 110% and 45%, respectively. Here, the thin film structures have a thickness of  $\delta = 100 \mu\text{m}$ , an inner diameter of  $D_i = 10.0 \text{ mm}$ , and a height of  $2.0 \leq h \leq 8.0 \text{ mm}$ .
- (2) For ETFS, with increasing temperature of base surface, three mixed boiling modes successively appear in the pool: nuclear boiling/convection (NB/C), partial film boiling/nuclear boiling (PFB/NB), and film boiling/nuclear boiling (FB/NB). Through visualization and infrared temperature measurement techniques, it was found that nucleate boiling in the falling liquid film on extended surface is the key to stabilizing the surface temperature during the formation of dry spots on the base surface. At high heat flux, the mutual interference between nucleate boiling and film boiling effectively inhibits the heat transfer deterioration caused by the deactivation of a large area of nucleation sites on the base surface, and delays the occurrence of CHF.
- (3) Extended film height has an important effect on the mutual interference between base surface and extended surface in the pool. Two different reasons are provided to elucidate the effect of height on CHF: a small height will reduce the temperature difference between the extended surface and the base surface, making it difficult to maintain mixed boiling in the pool. A large height increases the resistance of cold liquid entering the pool along the extended film, and the evaporation drying of partially extended surfaces weakens the mutual interference between nuclear boiling and film boiling in the mixed boiling. Therefore, for ETFS, the optimal height for improving CHF is 4.0 mm.
- (4) The ratio factor  $RF_\alpha$  is introduced to characterize the roles of the extended surface in enhancing heat transfer performance. The main reason for enhancing CHF on ETFS is not the tip cooling of extended surface, but the cooperative competition effect between the extended surface and base surface. The contribution of the extended surface to enhancing heat transfer is obtained by decoupling the mutual interference process in mixed boiling. For  $h = 2.0, 4.0, 6.0, \text{ and } 8.0 \text{ mm}$ , the contributions of the extended surface to the total heat transfer are 12%, 64%, 37%, and 24%, respectively, which aligns well with the optimal height of 4.0 mm for extended film structure.

## ACKNOWLEDGMENTS

The authors acknowledge the support from the National Natural Science Foundation of China (Grant Nos. 52176154 and 52130608).

## AUTHOR DECLARATIONS

### Conflict of Interest

The authors have no conflicts to disclose.

### Author Contributions

**Hao Wang:** Conceptualization (equal); Data curation (equal); Formal analysis (lead); Investigation (lead); Methodology (lead); Writing – original draft (lead); Writing – review & editing (equal). **Dongxue Guan:** Data curation (equal); Formal analysis (supporting); Investigation (supporting). **Xianbing Ji:** Funding acquisition (lead); Resources (equal); Supervision (equal); Validation (equal); Writing – review & editing (lead). **Jinliang Xu:** Conceptualization (lead); Funding acquisition (lead); Project administration (lead); Resources (equal); Supervision (equal); Validation (equal).

### DATA AVAILABILITY

The data that support the findings of this study are available from the corresponding author upon reasonable request.

## NOMENCLATURE

### Symbols

$Bi$	biot number
$c_{p,1}$	specific heat capacity of liquid, J/(kg K)
$C_{s,1}$	coefficient factor
$D$	diameter (m)
$D_b$	bubble departure diameter
$g$	gravity acceleration ( $\text{m/s}^2$ )
$h$	height of extend surface (m)
$h_{fg}$	latent heat of evaporation (J/kg)
$l_c$	capillary length (m)
$l_{ta}$	Taylor wavelength (m)
$m$	the quality of liquid film (kg)
$Pr$	Prandtl number
$Q$	quantity of heat (J)
$q$	heat flux ( $\text{W/m}^2$ )
$R_v$	effective thermal resistance of vapor (K/W)
$RF_\alpha$	enhanced heat transfer factor
$RF_\alpha$	ratio factor in enhancing heat transfer performance
$t$	time (s)
$T$	temperature ( $^\circ\text{C}$ )
$T_{w,r}$	temperature at the root of extended film ( $^\circ\text{C}$ )
$u$	speed (m/s)
$\Delta s$	effective width for IR temperature measurement (pix)
$\Delta T$	temperature difference ( $^\circ\text{C}$ )
$\Delta z$	the test section's temperature measuring intervals (m)

### Greek symbol

$\alpha$	heat transfer coefficient ( $\text{W}/(\text{m}^2 \text{ K})$ )
$\beta$	static contact angle (deg)
$\delta$	the thickness of extended surface (m)
$\delta_T$	the thickness of thermal boundary layer (m)
$\eta$	viscosity (Pa s)

$\lambda$	thermal conductivity (W/(m <sup>2</sup> K))
$\rho$	density (kg/m <sup>3</sup> )
$\sigma$	surface tension (N/m)
$\sigma_T$	temperature standard deviation of base surface rim
$\tau$	viscous shear force (N)

### Subscripts

b	boiling base surface
dry	dry spot
e	extended thin film surface
f	fluid
i	inside of the extended surface
l	liquid phase
o	outside of the extended surface
r	root of the extended film
sat	saturation temperature
v	vapor phase

### Acronym

C	convective heat transfer
CHF	critical heat flux
ETFS	extended thin film surface
FB	film boiling
FPS	pin–fin surface
NB	nucleate boiling
PS	plain surface

### REFERENCES

- M. Zeng, S. C. Wang, J. H. Duan, J. H. Sun, P. Y. Zhong, and Y. J. Zhang, “Review of nuclear power development in China: Environment analysis, historical stages, development status, problems and countermeasures,” *Renewable Sustainable Energy Rev.* **59**, 1369 (2016).
- B. Zhu, J. Xu, H. Zhang, J. Xie, and M. Li, “Effect of non-uniform heating on scCO<sub>2</sub> heat transfer deterioration,” *Appl. Therm. Eng.* **181**, 115967 (2020).
- G. T. Liang and I. Mudawar, “Review of pool boiling enhancement by surface modification,” *Int. J. Heat Mass Transfer* **128**, 892 (2019).
- S. Nukiyama, “The maximum and minimum values of the heat Q transmitted from metal to boiling water under atmospheric pressure,” *Int. J. Heat Mass Transfer* **9**, 1419 (1966).
- S. K. Singh and D. Sharma, “Review of pool and flow boiling heat transfer enhancement through surface modification,” *Int. J. Heat Mass Transfer* **181**, 122020 (2021).
- C. Wang, M. M. Rahman, and M. Bucci, “Decrypting the mechanisms of wicking and evaporation heat transfer on micro-pillars during the pool boiling of water using high-resolution infrared thermometry,” *Phys. Fluids* **35**, 037112 (2023).
- R. Pastuszko, R. Kaniowski, and T. M. Wojcik, “Comparison of pool boiling performance for plain micro-fins and micro-fins with a porous layer,” *Appl. Therm. Eng.* **166**, 114658 (2020).
- Y. H. Zhang, J. Zhou, W. J. Zhou, B. J. Qi, and J. J. Wei, “CHF correlation of boiling in FC-72 with micro-pin-fins for electronics cooling,” *Appl. Therm. Eng.* **138**, 494 (2018).
- A. Q. Lou, H. Y. Wang, and L. Li, “A lattice Boltzmann investigation of the saturated pool boiling heat transfer on micro-cavity/fin surfaces,” *Phys. Fluids* **35**, 013316 (2023).
- M. S. El-Genk and A. Suszko, “Effects of inclination angle and liquid subcooling on nucleate boiling on dimpled copper surfaces,” *Int. J. Heat Mass Transfer* **95**, 650 (2016).
- A. K. Das, P. K. Das, and P. Saha, “Nucleate boiling of water from plain and structured surfaces,” *Exp. Therm. Fluid Sci.* **31**, 967 (2007).
- M. M. Rahman, E. Olceroglu, and M. McCarthy, “Scalable nanomanufacturing of virus-templated coatings for enhanced boiling,” *Adv. Mater. Interfaces* **1**, 1300107 (2014).
- Y. Y. Hsu, “On the size range of active nucleation cavities on a heating surface,” *J. Heat Transfer* **84**, 207 (1962).
- S. M. Kwark, G. Moreno, R. Kumar, H. Moon, and S. M. You, “Nanocoating characterization in pool boiling heat transfer of pure water,” *Int. J. Heat Mass Transfer* **53**, 4579 (2010).
- H. S. Jo, T. G. Kim, J. G. Lee, M. W. Kim, H. G. Park, S. C. James, J. Choi, and S. S. Yoon, “Supersonically sprayed nanotextured surfaces with silver nanowires for enhanced pool boiling,” *Int. J. Heat Mass Transfer* **123**, 397 (2018).
- S. Das, D. S. Kumar, and S. Bhaumik, “Experimental study of nucleate pool boiling heat transfer of water on silicon oxide nanoparticle coated copper heating surface,” *Appl. Therm. Eng.* **96**, 555 (2016).
- S. Sinha-Ray, W. S. Zhang, R. P. Sahu, S. Sinha-Ray, and A. L. Yarin, “Pool boiling of Novec 7300 and DI water on nano-textured heater covered with supersonically-blown or electrospun polymer nanofibers,” *Int. J. Heat Mass Transfer* **106**, 482 (2017).
- C. Y. Lee, B. J. Zhang, and K. J. Kim, “Morphological change of plain and nano-porous surfaces during boiling and its effect on nucleate pool boiling heat transfer,” *Exp. Therm. Fluid Sci.* **40**, 150 (2012).
- D. X. Deng, J. Y. Feng, Q. S. Huang, Y. Tang, and Y. S. Lian, “Pool boiling heat transfer of porous structures with reentrant cavities,” *Int. J. Heat Mass Transfer* **99**, 556 (2016).
- C. Shen, C. C. Zhang, Y. C. Bao, X. B. Wang, Y. Liu, and L. Q. Ren, “Experimental investigation on enhancement of nucleate pool boiling heat transfer using hybrid wetting pillar surface at low heat fluxes,” *Int. J. Therm. Sci.* **130**, 47 (2018).
- Q. Li, Y. Yu, P. Zhou, and H. J. Yan, “Enhancement of boiling heat transfer using hydrophilic-hydrophobic mixed surfaces: A lattice Boltzmann study,” *Appl. Therm. Eng.* **132**, 490 (2018).
- M. M. Rahman, J. Pollack, and M. McCarthy, “Increasing boiling heat transfer using low conductivity materials,” *Sci. Rep.* **5**, 13145 (2015).
- Y. Utaka, T. X. Xie, Z. H. Chen, T. Morokuma, and H. Ohkubo, “Critical heat flux enhancement in narrow gaps via different-mode-interacting boiling with nonuniform thermal conductance inside heat transfer plate,” *Int. J. Heat Mass Transfer* **133**, 702 (2019).
- T. X. Xie, Y. Utaka, Z. H. Chen, T. Hirotsu, and S. Mori, “Effect of material arrangement pattern on different-mode-interacting boiling in narrow gaps with two liquid supply systems,” *Appl. Therm. Eng.* **191**, 116893 (2021).
- M. I. Omisanya, Z. H. Chen, and Y. Utaka, “Flow boiling critical heat flux enhancement via different-mode-interacting boiling in narrow gaps,” *Int. J. Heat Mass Transfer* **182**, 121982 (2022).
- B. Shen, J. W. Liu, G. Amberg, M. Do-Quang, J. Shiomi, K. Takahashi, and Y. Takata, “Contact-line behavior in boiling on a heterogeneous surface: Physical insights from diffuse-interface modeling,” *Phys. Rev. Fluids* **5**, 033603 (2020).
- C. L. Cao, X. J. Ma, J. L. Xu, H. W. Li, and G. L. Liu, “Explosive boiling induced fast transportation of Leidenfrost droplet to target location,” *Phys. Fluids* **34**, 053322 (2022).
- X. J. Ma, C. Q. Wang, and J. L. Xu, “Enhanced  $\gamma$ -component droplet motion via droplet-wall-contact induced explosive boiling on a convex surface,” *Phys. Fluids* **35**, 053320 (2023).
- D. E. Kim and J. Park, “Experimental study of critical heat flux in pool boiling using visible-ray optics,” *Int. J. Heat Mass Transfer* **169**, 120937 (2021).
- F. Tachibana, M. Akiyama, and H. Kawamura, “Non-hydrodynamic aspects of pool boiling burnout,” *J. Nucl. Sci. Technol.* **4**, 121 (1967).
- D. E. Kim, J. Song, and H. Kim, “Simultaneous observation of dynamics and thermal evolution of irreversible dry spot at critical heat flux in pool boiling,” *Int. J. Heat Mass Transfer* **99**, 409 (2016).
- J. H. Lienhard, V. K. Dhir, and D. M. Rihard, “Peak pool boiling heat-flux measurements on finite horizontal flat plates,” *J. Heat Transfer* **95**, 477 (1973).
- H. Wang, J. L. Xu, X. J. Ma, and J. Xie, “Evaporation of Leidenfrost droplet on thin soluble liquid bath with thermal non-equilibrium effect,” *Phys. Fluids* **34**, 093320 (2022).

- <sup>34</sup>S. Rout, R. K. Sahoo, and K. Chaudhury, "Measurement of the thermal diffusivities of insulating materials using boiling water," *Phys. Fluids* **35**, 077102 (2023).
- <sup>35</sup>H. W. Coleman and W. G. Steele, *Experimentation, Validation, and Uncertainty Analysis for Engineers* (John Wiley and Sons, 2018).
- <sup>36</sup>I. I. Pioro, "Experimental evaluation of constants for the Rohsenow pool boiling correlation," *Int. J. Heat Mass Transfer* **42**, 2003 (1999).
- <sup>37</sup>A. Bar-Cohen and A. McNeil, "Parametric effects on pool boiling critical heat flux in dielectric liquids," in *Proceedings of the Engineering Foundation Conference on Pool and External Flow Boiling* (ASME, Santa Barbara, CA, 1992).
- <sup>38</sup>K. N. Rainey and S. M. You, "Effects of heater size and orientation on pool boiling heat transfer from microporous coated surfaces," *Int. J. Heat Mass Transfer* **44**, 2589 (2001).
- <sup>39</sup>H. Z. Bian, C. Kurwitz, Z. N. Sun, K. Cheng, and K. L. Chen, "Enhanced nucleate boiling on 3D-printed micro-porous structured surface," *Appl. Therm. Eng.* **141**, 422 (2018).
- <sup>40</sup>C. K. Yu and D. C. Lu, "Pool boiling heat transfer on horizontal rectangular fin array in saturated FC-72," *Int. J. Heat Mass Transfer* **50**, 3624 (2007).
- <sup>41</sup>K. N. Rainey and S. M. You, "Pool boiling heat transfer from plain and microporous, square pin-finned surfaces in saturated FC-72," *J. Heat Transfer* **122**, 509 (2000).
- <sup>42</sup>L. L. Yuan, F. J. Hong, and P. Cheng, "Pool boiling enhancement through a guidance structure mounted above heating surface," *Int. J. Heat Mass Transfer* **139**, 751 (2019).
- <sup>43</sup>Z. Zhou, J. X. Shi, H. H. Chen, S. R. Schafer, and C. L. Chen, "Two-phase flow over flooded micro-pillar structures with engineered wettability pattern," *Int. J. Heat Mass Transfer* **71**, 593 (2014).
- <sup>44</sup>C. L. Tien, "A hydrodynamic model for nucleate pool boiling," *Int. J. Heat Mass Transfer* **5**, 533 (1962).
- <sup>45</sup>H. X. Chen, Y. Sun, L. H. Li, and X. D. Wang, "Bubble dynamics and heat transfer performance on micro-pillars structured surfaces with various pillars heights," *Int. J. Heat Mass Transfer* **163**, 120502 (2020).
- <sup>46</sup>X. T. Chang, H. B. Huang, Y. P. Cheng, and X. Y. Lu, "Lattice Boltzmann study of pool boiling heat transfer enhancement on structured surfaces," *Int. J. Heat Mass Transfer* **139**, 588 (2019).
- <sup>47</sup>Z. C. Zhao, X. L. Ma, S. L. Li, S. Yang, and L. Q. Huang, "Visualization-based nucleate pool boiling heat transfer enhancement on different sizes of square micropillar array surfaces," *Exp. Therm. Fluid Sci.* **119**, 110212 (2020).
- <sup>48</sup>B. Shen, T. Hamazaki, W. Ma, N. Iwata, S. Hidaka, A. Takahara, K. Takahashi, and Y. Takata, "Enhanced pool boiling of ethanol on wettability-patterned surfaces," *Appl. Therm. Eng.* **149**, 325 (2019).
- <sup>49</sup>T. L. Bergman, T. L. Bergman, F. P. Incropera, D. P. Dewitt, and A. S. Lavine, *Fundamentals of Heat and Mass Transfer* (John Wiley and Sons, 2011).
- <sup>50</sup>I. C. Chu, H. C. No, and C. H. Song, "Visualization of boiling structure and critical heat flux phenomenon for a narrow heating surface in a horizontal pool of saturated water," *Int. J. Heat Mass Transfer* **62**, 142 (2013).
- <sup>51</sup>X. Li, X. Fang, Y. Guo, P. Yang, and Z. He, "Experimental study on subcooled pool boiling heat transfer of sodium dodecyl sulfate surfactant solution," *Phys. Fluids* **35**, 023307 (2023).
- <sup>52</sup>H. S. Ahn and M. H. Kim, "Visualization study of critical heat flux mechanism on a small and horizontal copper heater," *Int. J. Multiphase Flow* **41**, 1–12 (2012).
- <sup>53</sup>I. C. Chu, H. C. No, C. H. Song, and D. J. Euh, "Observation of critical heat flux mechanism in horizontal pool boiling of saturated water," *Nucl. Eng. Des.* **279**, 189 (2014).
- <sup>54</sup>M. S. El-Genk and H. H. Saber, "Heat transfer correlations for liquid film in the evaporator of enclosed, gravity-assisted thermosyphons," *J. Heat Transfer* **120**, 477 (1998).
- <sup>55</sup>H. Y. Zhao and A. Williams, "Predicting the critical heat flux in pool boiling based on hydrodynamic instability induced irreversible hot spots," *Int. J. Multiphase Flow* **104**, 174 (2018).
- <sup>56</sup>S. Jung and H. Kim, "Observation of the mechanism triggering critical heat flux in pool boiling of saturated water under atmospheric pressure," *Int. J. Heat Mass Transfer* **128**, 229 (2019).
- <sup>57</sup>Z. Z. Cao, J. Zhou, J. J. Wei, D. L. Sun, and B. Yu, "Direct numerical simulation of bubble dynamics and heat transfer during nucleate boiling on the micro-pin-finned surfaces," *Int. J. Heat Mass Transfer* **163**, 120504 (2020).
- <sup>58</sup>K. N. Rainey, S. M. You, and S. Lee, "Effect of pressure, subcooling, and dissolved gas on pool boiling heat transfer from microporous, square pin-finned surfaces in FC-72," *Int. J. Heat Mass Transfer* **46**, 23 (2003).
- <sup>59</sup>Y. Li, W. Li, J. Xie, J. Xu, and Z. Miao, "Eliminating flooding by phase separation in condenser tube," *Phys. Fluids* **34**, 123310 (2022).